Soft phonon mode as the origin of the reduced thermal conductivity in Ta-based trirutiles

R. Tartaglia,[1] A. F. Lima,[2] N. Prasai,[3] A. B. Christian,[4] J. J. Neumeier,[4] J. L. Cohn,[3] and E. Granado[1]
[1)] *Universidade Estatual de Campinas (UNICAMP), Instituto de Física Gleb Wataghin, Campinas, São Paulo 13083-859, Brazil*[a)]
[2)] *Departamento de Física do Campus de Itabaiana, Universidade Federal de Sergipe, Itabaiana, Sergipe 49510-200, Brazil*
[3)] *Department of Physics, University of Miami, Coral Gables, Florida 33124, USA*
[4)] *Department of Physics, Montana State University, Bozeman, Montana 59717, USA*

(*Electronic mail: rodolfo.souza@lnls.br)

Ta-based trirutiles of the series ATa_2O_6 (A = Ni, Co) reportedly present suppressed thermal conductivity (κ) values compared to their Sb-based counterparts. Particularly, the κ values at room temperature for Ta-based samples are in the range observed in materials already employed as thermoelectric devices, suggesting they are potential candidates as a starting point for thermoelectric applications. Here, we investigate their phonon dynamics through a combination of Raman scattering measurements with density functional theory (DFT) calculations. For the Ta-based compounds only, our results reveal the presence of an E_g low-energy optical phonon that softens by ~ 10 cm^{-1} upon cooling from 300 K to 15 K, indicating this is a zone-center soft mode associated with an unrealized structural phase transition. The soft mode enhances the phonon density of states at low energies, as directly manifested in the second-order Raman scattering data and also captured by DFT phonon calculations. These results provide insights into the low κ-values of Ta-based trirutiles and places zone-center soft phonons as a key ingredient for the development of novel thermoelectic materials.

Thermoelectric materials can convert heat, including waste heat, into electricity and vice-versa without greenhouse emissions, making them proper candidates for sustainable energy solutions[1,2]. Their efficiency in energy conversion is quantified by the dimensionless figure of merit, $ZT = \sigma S^2 T/\kappa$, where σ is the electrical conductivity, S is the Seebeck coefficient, T is the absolute temperature, and κ is the thermal conductivity. The main drawback concerning their applicability is the complex interplay between σ, S, and κ, which imposes significant difficulties when attempting to increase ZT[3,4]. In this regard, a promising strategy is to explore compounds that have intrinsically low thermal conductivity and try to enhance the other two parameters[1–4].

In the range of temperatures where thermoelectric materials are employed, phonons are the primary heat carriers[5,6]. Therefore, compounds where phonons are strongly scattered are potential candidates for application as thermoelectric devices[7]. In this context, three classes of compounds call for attention: the clathrates, skutterudites, and IV-VI chalcogenides[8]. For all of them, the observed low thermal conductivity originates from the unusual presence of a low-energy optical phonon mode and its interaction with the acoustic branch[9–20].

In this context, another noteworthy class of compounds is the family AB_2O_6 (A = Co, Ni, Cu; B = Sb, Ta), crystallizing in the trirutile structure with the tetragonal space group $P4_2/mnm$[21–25]. Much of the interest in these systems concerns their magnetic properties. For all of them, one-dimensional spin chains of transition metal ions exhibit long-range antiferromagnetic ordering, with short-range correlations starting well above T_N[21–25], offering a rich platform to study magnetic interactions in reduced dimensions. Besides those appealing magnetic properties, these compounds also display an intricate behavior in their thermal properties[26]. Compounds with Ta exhibit κ values at room temperature comparable to those found in materials already used as thermoelectric devices[2,3,26]. In addition, comparing the thermal conductivity between Ta- and Sb-based trirutiles, a suppression of about one order of magnitude is observed for the samples with Ta, regardless of the transition metal ion at the A site[26]. Employing the Callaway model and considering the scattering of acoustic phonons by point defects, dislocations, boundaries, and Umklapp processes is sufficient to reproduce the thermal conductivity of $NiSb_2O_6$[26]. For $NiTa_2O_6$, besides those processes, an additional scattering mechanism from optical phonons must be invoked[26]. Thus, a possible proximity of an optical phonon with the acoustic branch remains elusive and calls for an experimental verification.

In this work, we investigate the origin of the suppressed thermal conductivity in Ta-based trirutiles with respect to their Sb counterparts in the AB_2O_6 family (A = Ni, Co, Zn; B = Sb, Ta) by combining temperature-dependent Raman spectroscopy measurements in the paramagnetic phase with density functional theory (DFT) calculations. We found that the Ta-based samples have a low-energy optical phonon that softens throughout the entire measured temperature range, suggesting an incipient soft-mode driven structural instability. The presence of this optical mode provides additional decay channels for the heat-carrying acoustic phonons, yielding insights into the microscopic origin of the thermal properties of these compounds.

Figures 1(a) and 1(b) exhibit the low-frequency region of the calculated phonon dispersions for $NiTa_2O_6$ and $NiSb_2O_6$, (for more details about the DFT calculations, see Section S1 in the Supplementary Material), respectively, highlighting the

[a)] Present address: Brazilian Synchrotron Light Laboratory (LNLS), Brazilian Center for Research in Energy and Materials (CNPEM), Campinas, São Paulo 13083-970, Brazil

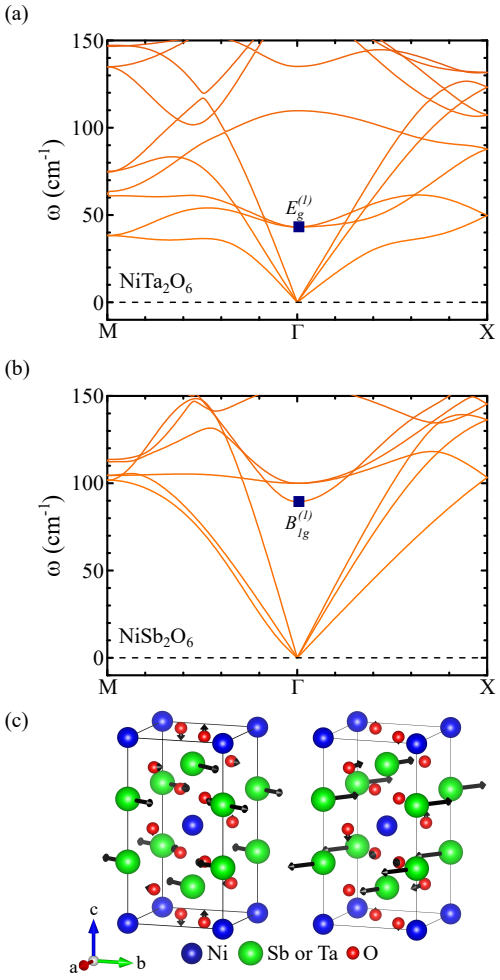

FIG. 1. Phonon dispersion relation along $M-\Gamma-X$ directions of the Brillouin zone for (a) $NiTa_2O_6$ and (b) $NiSb_2O_6$ only showing the low-frequency region. Blue squares indicate the lowest optical phonon mode in both panels. (c) Mechanical representation of the doubly-degenerate $E_g^{(1)}$ mode, with black arrows indicating the direction of the vibration.

behavior of the acoustic and the less energetic optical phonon branches. Remarkably, $NiTa_2O_6$ presents a low-frequency optical phonon at the Γ point (calculated $\omega = 43$ cm^{-1}), which is the $E_g^{(1)}$ Raman-active doubly degenerate mode [see Table S2 in the Supplementary Material and Fig. 1(c) for its mechanical representation]. $NiSb_2O_6$, on the other hand, displays its lowest-frequency optical mode at 89 cm^{-1}, which is a nondegenerate B_{1g} mode, while the $E_g^{(1)}$ mode occurs at 100 cm^{-1}. Close to the Γ-point, the dispersions of the three acoustic branches are similar for both compounds. However, at the M and X points, the acoustic modes for the Ta-based compound are softer by a factor of two or more with respect to $NiSb_2O_6$.

We proceed to the theoretical ph-DOS, shown in Figs. 2(a) and 2(b). For $NiTa_2O_6$ [Fig. 2(a)], a substantial ph-DOS is noticed for 2ω between ~ 60 and 140 cm^{-1}, which originates from both the low-frequency optical and the acoustic branches [Fig. 1(a)]. For $NiSb_2O_6$ [Fig. 2(b)], the ph-DOS remains quite small for $2\omega < 150$ cm^{-1}, as could be anticipated from the absence of an optical mode in this frequency region and the much wider dispersion of the acoustic branches in comparison with the Ta-based compound [Fig. 1(b)].

Figures 2(c) and 2(d) display the experimental low-ω Raman response of $NiTa_2O_6$ and $NiSb_2O_6$ (for more details about the sample growth methods and Raman spectroscopy measurements, see Sections S2 and S3, respectively, in the Supplementary Material), respectively, at $T = 15$ K. For $NiTa_2O_6$, two first-order modes are observed at $\omega = 29$ cm^{-1} and 128 cm^{-1} and assigned as $E_g^{(1)}$ and $B_{1g}^{(1)}$ modes, respectively (see Table S2 in the Supplementary Material). A broad scattering is also detected for ω between 50 and 120 cm^{-1}, characteristic of second-order Raman process. In addition, the shape of this signal shows a close correspondence with the calculated ph-DOS in Fig. 2(a), supporting its assignment to two-phonon Raman scattering. This method is a well-known probe of the ph-DOS[28?–30].

The thermal evolution of the low-ω Raman signal of $NiTa_2O_6$ is presented in Fig. 3(a). Remarkably, the $E_g^{(1)}$ mode shows a substantial hardening from 29 cm^{-1} at $T = 15$ K to 39 cm^{-1} at $T = 290$ K. This is the opposite trend of conventional behavior, where the volume expansion associated with the cubic anharmonic term of the interatomic potential promotes a slight softening of the vibrations upon warming[31–33]. In the present case, the strong temperature dependence of the $E_g^{(1)}$ frequency is indicative of a soft mode behavior that occurs in the vicinity of displacive structural phase transitions[34–36], where the soft mode frequency behaves as an order parameter of the transition and follows Cochran's equation $\omega \propto (T - T_c)^{1/2}$ (Ref. 27). Using this expression to fit our data [see Fig. 3(c)], we obtain $T_c = -341$ K for $NiTa_2O_6$. This negative value for T_c indicates an unrealized structural phase transition. The other investigated Ta-based compound, $CoTa_2O_6$, presents similar results, except that the $E_g^{(1)}$ mode is harder in this case, indicating that this compound is farther away from the structural phase transition with $T_c = -471$ K [see Figs. 3(b) and 3(c)].

Further information about the crystal structure dynamics of these materials is obtained by examining the high-ω modes, which are associated with oxygen vibrations. The symmetry analysis and phonon assignments are provided in the Supplementary Material (see Tables S1 and S2). Figures 4(a) - 4(d) display the Raman response at selected temperatures for $NiTa_2O_6$, $CoTa_2O_6$, $NiSb_2O_6$, and $ZnSb_2O_6$, respectively. It is possible to notice that the high-ω modes of ATa_2O_6 (A =

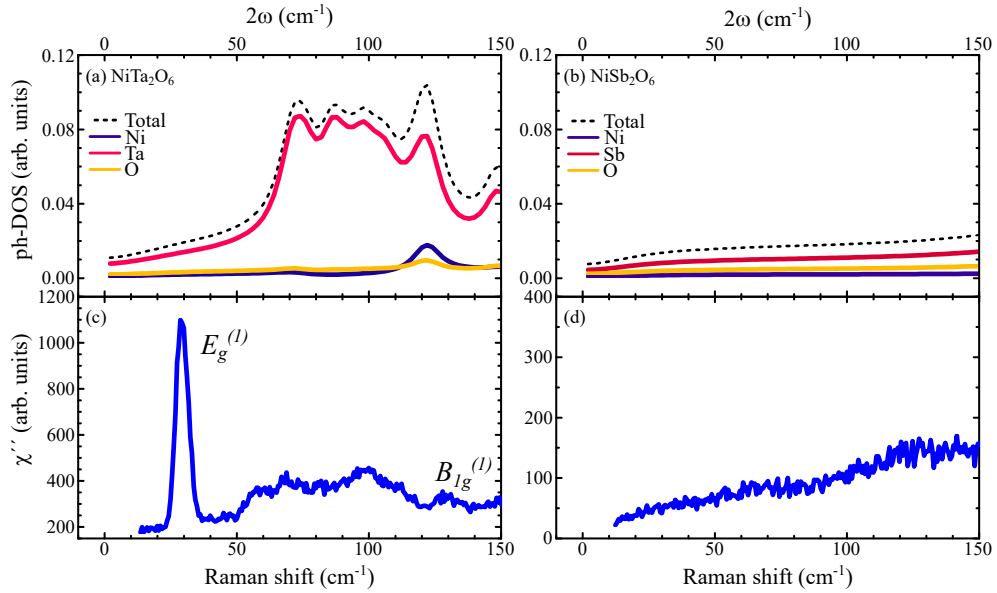

FIG. 2. Calculated phonon density of states for (a) $NiTa_2O_6$ and (b) $NiSb_2O_6$. Raman response measured at 15 K for (c) $NiTa_2O_6$ and (d) $NiSb_2O_6$.

Ni, Co) show a more pronounced broadening upon warming than the Sb-based compounds. We investigate in more detail the $A_{1g}^{(4)}$ mode at $\omega \sim 680-750$ cm^{-1}, highlighted with an asterisk in Figs. 4(a) - 4(d). The mechanical representation of this particular mode is indicated in Fig. 5(a). Figures 5(b) - 5(e) show the temperature-dependence of its linewidth (Γ) for the compounds studied in this work. For Sb-based compounds, the phonon broadening is well captured by a conventional two-phonon decay model $\Gamma(T) = \Gamma_0[1 + 2/(e^x - 1)]$, where $x \equiv \hbar\omega_0/k_bT$ (refs. 32 and 37). However, for Ta-based compounds, the thermal broadening effect is much larger than predicted by this model at $T \gtrsim 30$ K. Although this is a simplified model, this comparison clearly indicates that an additional source of anharmonicity, not present in the investigated Sb-based compounds, is responsible for the reduced lifetime of the high-frequency optical modes for the Ta-based materials.

In ordered magnetic materials, phonon frequencies can also be renormalized through spin-phonon coupling at characteristic temperatures associated with the onset of long-range magnetic ordering[38] or short-range magnetic correlations[39,40]. This raises the question of whether spin degrees of freedom contribute to the temperature dependence observed for the E_g mode. All the Raman measurements in this study were conducted above the Néel temperature of the compounds[21–25]. In addition, short-range correlations in all cases extend up to 30 K[21–25]. Since the E_g mode softens across the entire temperature range, with no apparent change at those temperatures, the spin-phonon coupling is not significant for the underlying physics of the E_g mode. Instead, its behavior is of anharmonic origin.

The pronounced temperature-induced renormalization of the $E_g^{(1)}$ phonon frequency implies a strongly anharmonic interatomic potential as a function of the corresponding normal coordinate in ATa_2O_6 (A = Ni and Co). Its temperature-dependence indicates this is the soft mode of an unrealized symmetry-breaking instability, placing them in the vicinity of a symmetry-lowering structural phase transition. The negative transition temperatures from Cochran's equation[27] found here for $NiTa_2O_6$ ($T_c = -341$ K) and $CoTa_2O_6$ ($T_c = -471$ K) are characteristic of incipient ferroelectric materials. Typical examples are TiO_2[41], with $T_c = -540$ K[42–45], and PbTe, with T_c ranging from -151 K to -79 K[46–48]. In the present case, we stress that the soft mode is a Raman-active E_g mode that is not associated with an oscilating electric dipole. Therefore, the presumed structural transition associated with this mode retains the inversion center and, thus, cannot be associated with a ferroelectric state.

Incipient ordering, as shown here for Ta-based compounds, indicates some mechanism is pushing the material away from the critical point. As mentioned before, this is the case of PbTe, which lies close to a ferroelectric order, and a small amount of Ge doping on the Pb site can induce the ferroelectric state[49]. Therefore, it remains to be determined which kind of ordering could emerge in samples with Ta if the E_g mode softens entirely. In this regard, external pressure is a natural

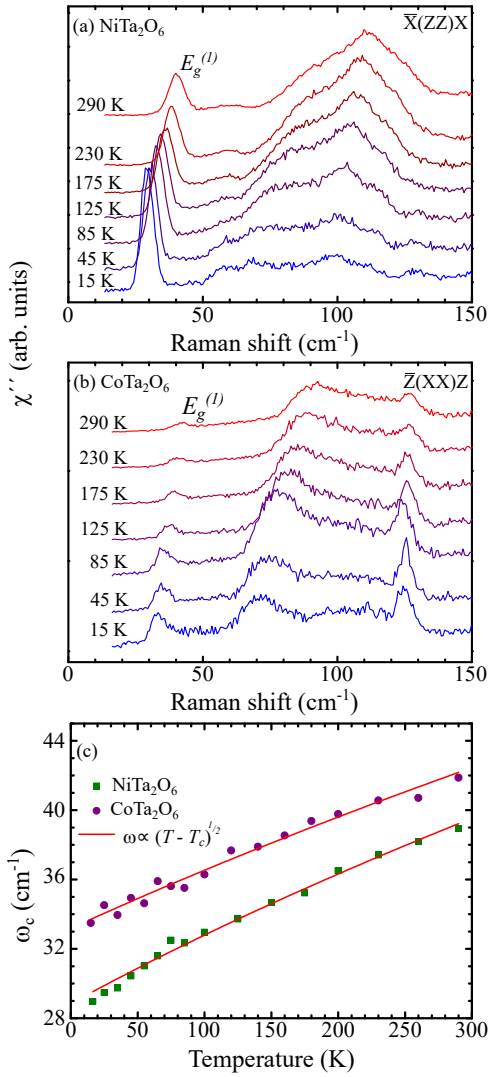

FIG. 3. Raman response of the low-frequency region ($\omega < 150$ cm^{-1}) at selected temperatures for (a) $NiTa_2O_6$ and (b) $CoTa_2O_6$. (c) $E_g^{(1)}$ peak position as a function of temperature for $NiTa_2O_6$ (green squares) and $CoTa_2O_6$ (purple circles). The red lines correspond to fits with the function $\omega \propto (T - T_c)^{\frac{1}{2}}$, where T_c denotes the transition temperature to a lower-symmetry structure[27].

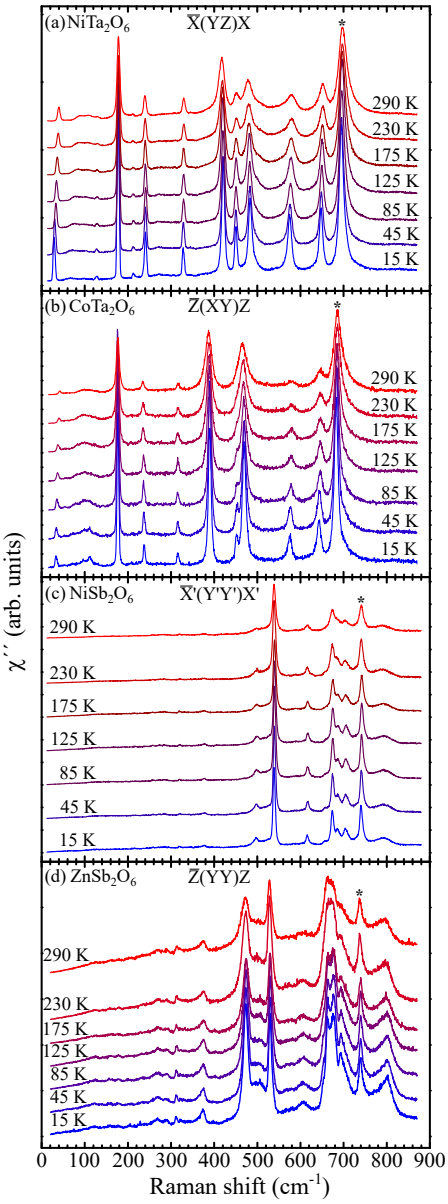

FIG. 4. Raman response at selected temperatures for (a) $NiTa_2O_6$, (b) $CoTa_2O_6$, (c) $NiSb_2O_6$, (d) and $ZnSb_2O_6$. The asterisk in each panel highlights the $A_{1g}^{(4)}$ mode.

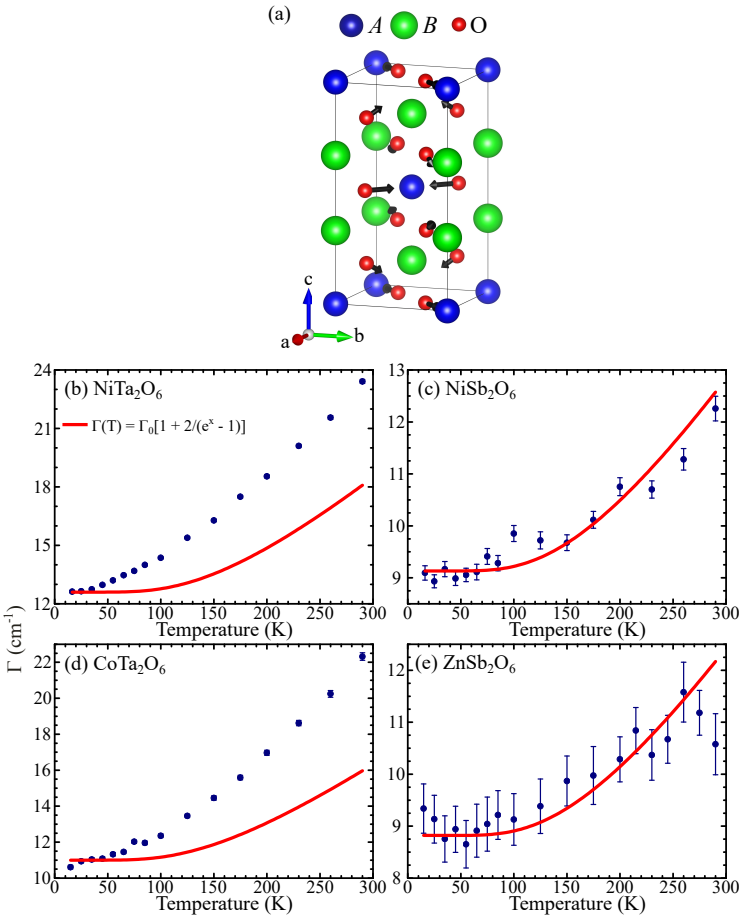

FIG. 5. (a) Mechanical representation of the $A_{1g}^{(4)}$ mode, with black arrows indicating the direction of the vibration. Width (Γ) of the $A_{1g}^{(4)}$ mode as a function of temperature for (b) $NiTa_2O_6$, (c) $NiSb_2O_6$, (d) $CoTa_2O_6$, and (e) $ZnSb_2O_6$. Red curves are fits with the function $\Gamma(T) = \Gamma_0[1+2/(e^x-1)]$, where $x \equiv \hbar\omega_0/k_bT$ (ref. 32).

way to shed light on this scenario. Recent Raman and x-ray diffraction measurements on polycrystalline $NiTa_2O_6$ at room temperature up to 25 GPa revealed a structural phase transition near 12 GPa to a lower-symmetry crystal structure[50]. However, due to experimental constraints, the low-frequency region containing the $E_g^{(1)}$ mode was not probed as a function of pressure. Thus, the pressure dependence of the soft mode remains unknown, and future Raman experiments under pressure at different temperatures are demanded. This will enable the study of whether the structural phase transition is driven by the soft mode and also how pressure influences the anharmonic interactions in Ta-based analogs.

Most materials with noticeably low κ-values have in common one or more low-ω optical phonon branches that interact with the acoustic ones[9–16]. As demonstrated here, this is also the case for the Ta-based trirutiles [see Fig. 1(a)]. In contrast, the lowest optical phonon mode in $NiSb_2O_6$ is nearly twice as high in energy as in its Ta-based counterpart [see Figs. 1(a) and 1(b)]. As a result, the additional scattering mechanism of the heat-carrying acoustic phonons by an optical mode plays a significant role in the thermal conductivity of compounds with Ta, while it might contribute only marginally for Sb-based analogs. This interaction manifests in samples with Ta as a two-phonon Raman signal [see Figs. 2(c) and 2(d)] and is evidenced by its temperature dependence. Since this sig-

nal contains contributions from the acoustic branches and the $E_g^{(1)}$ soft mode [see Figs. 2(a) and 2(c)], as the latter hardens upon warming, the two-phonon Raman signal also shifts its spectral weight to higher frequencies [see Figs. 3(a) and 3(b)]. Therefore, as suggested by previous thermal conductivity measurements[26] and supported by our findings, the coupling between acoustic and low-ω optical phonon branches appears to be a decisive ingredient for the low thermal conductivity of the Ta-based compounds.

The large difference between the κ values of the Ta- and Sb-based trirutiles[26], even though they have the same crystal structure, is remarkable. The strong anharmonic interactions revealed by the presence of a soft mode appear to be the root of this contrast. This is further evidenced by the significant broadening of high-ω phonons upon warming in the Ta-based compounds [see Figs. 5(b) and 5(d)]. For insulator compounds in the paramagnetic regime, phonon-phonon decay is the major source of line broadening and serves as an indirect tool to study the degree of anharmonicity in the crystal structure. Strong anharmonicity can be considered when phonon broadening deviates from the two-phonon decay model[32,37]. As shown in Figs. 5(b) and 5(d), the Sb-based compounds are well described by this model, while for the samples with Ta, the curve fails to reproduce the experimental data [see Figs. 5(b) and 5(d)]. Thus, as the thermal population of the $E_g^{(1)}$ soft mode becomes appreciable ($T \gtrsim 30$ K), the broadening of the high-ω modes deviates from the conventional anharmonic behavior found in Sb-based compounds. It is apparent that the slow dynamics of the low-ω $E_g^{(1)}$ soft mode are sensed by the faster high-ω modes as an effective structural disorder[51–54].

The association of the low thermal conductivity with a soft mode driven by anharmonicity opens the possibility to control κ by tuning the soft mode frequency through external parameters. In addition to pressure, as already commented, strain or chemical substitution are other effective tools for modifying physical properties. The latter is particularly relevant for thermoelectric materials, which, besides the low κ-values, should also present good electrical conductivity and large Seebeck coefficients. Thus, it would be interesting to evaluate whether the Ta-based trirutiles may become efficient thermoelectric materials under electronic doping, which also produces chemical pressure. If this is the case, the possible κ-tuning could boost the development of novel thermoelectric devices.

In summary, we conducted a detailed investigation of the lattice dynamics in trirutile compounds AB_2O_6 (A = Ni, Co, Zn; B = Sb, Ta) employing Raman spectroscopy measurements supported by DFT calculations. We demonstrate the existence of a low-ω phonon branch in ATa_2O_6 derived from a soft E_g mode. Its presence indicates an incipient instability in the crystal structure due to strong anharmonic contributions to the interatomic potentials. Moreover, we calculate and observe a high density of phonon states at low energies for the Ta-based trirutiles. The effective dynamical structural disorder induced by the thermal population of the soft mode appears to reduce the other phonons' lifetimes. These results not only provide insights into the low κ-values of Ta-based trirutiles in comparison to the Sb-based ones, but also indicate that compounds with phonon anharmonicity strong enough to induce zone-center soft modes is a promissing avenue for the discovery of novel thermoelectric materials.

SUPPLEMENTARY MATERIAL

See the supplementary material for detailed information on DFT calculations, sample growth, Raman spectroscopy measurements, symmetry analysis, and phonon assignments.

We acknowledge the support of the INCT project Advanced Quantum Materials, involving the Brazilian agencies CNPq (Proc. 408766/2024-7), FAPESP, and CAPES. Work at UNICAMP was also supported by FAPESP Grants 2019/10401-9 and 2022/03539-7. Specimen preparation at the Univ. Miami was supported by the U.S. DOE, Office of Basic Energy Sciences, Div. of Mater. Sci. and Eng., under grant No. DE-SC0008607.

AUTHOR DECLARATIONS

Conflict of Interest

The authors have no conflicts to disclose.

Author Contributions

R. Tartaglia: Conceptualization (supporting); Data Curation (supporting); Formal Analysis (lead); Investigation (lead), Writing – original draft (lead). **A. F. Lima:** Data Curation (lead); Investigation (supporting); Writing – original draft (supporting); **N. Prasai**: Investigation (equal). **A. B. Christian**: Investigation (equal). **J. J. Neumeier**: Supervision (equal); Writing – review & editing (supporting). **J. L. Cohn**: Supervision (equal); Writing – review & editing (supporting). **E. Granado**: Conceptualization (leading); Supervision (lead); Writing – review & editing (lead).

DATA AVAILABILITY STATEMENT

The data that support the findings of this study are available within the article.

[1] J. He and T. M. Tritt, "Advances in thermoelectric materials research: Looking back and moving forward," Science **357**, eaak9997 (2017).
[2] X. Zhou, Y. Yan, X. Lu, H. Zhu, X. Han, G. Chen, and Z. Ren, "Routes for high-performance thermoelectric materials," Materials Today **21**, 974–988 (2018).
[3] L. C. X. Shi and C. Uher, "Recent advances in high-performance bulk thermoelectric materials," International Materials Reviews **61**, 379–415 (2016).
[4] S. K. Singh, J. Munevar, L. Mendonça-Ferreira, and M. A. Avila, "Next-Generation Quantum Materials for Thermoelectric Energy Conversion," Crystals **13** (2023), 10.3390/cryst13071139.
[5] T. M. Tritt, ed., Thermal conductivity, Physics of Solids and Liquids (Springer, New York, NY, 2004).
[6] F. Han, A Modern Course in the Quantum Theory of Solids (WORLD SCIENTIFIC, 2012).

[7] J. Yang, L. Xi, W. Qiu, L. Wu, X. Shi, L. Chen, J. Yang, W. Zhang, C. Uher, and D. J. Singh, "On the tuning of electrical and thermal transport in thermoelectrics: an integrated theory–experiment perspective," npj Computational Materials **2** (2016), 10.1038/npjcompumats.2015.15.
[8] M. d'Angelo, C. Galassi, and N. Lecis, "Thermoelectric Materials and Applications: A Review," Energies **16** (2023), 10.3390/en16176409.
[9] J. Dong, O. F. Sankey, and C. W. Myles, "Theoretical Study of the Lattice Thermal Conductivity in Ge Framework Semiconductors," Phys. Rev. Lett. **86**, 2361–2364 (2001).
[10] C. H. Lee, I. Hase, H. Sugawara, H. Yoshizawa, and H. Sato, "Low-Lying Optical Phonon Modes in the Filled Skutterudite $CeRu_4Sb_{12}$," Journal of the Physical Society of Japan **75**, 123602 (2006).
[11] M. Christensen, A. B. Abrahamsen, N. B. Christensen, F. Juranyi, N. H. Andersen, K. Lefmann, J. Andreasson, C. R. H. Bahl, and B. B. Iversen, "Avoided crossing of rattler modes in thermoelectric materials," Nature Materials **7**, 811–815 (2008).
[12] P. Norouzzadeh, C. W. Myles, and D. Vashaee, "Phonon dynamics in type-VIII silicon clathrates: Beyond the rattler concept," Phys. Rev. B **95**, 195206 (2017).
[13] T. Tadano, Y. Gohda, and S. Tsuneyuki, "Impact of Rattlers on Thermal Conductivity of a Thermoelectric Clathrate: A First-Principles Study," Phys. Rev. Lett. **114**, 095501 (2015).
[14] W. Li and N. Mingo, "Ultralow lattice thermal conductivity of the fully filled skutterudite $YbFe_4Sb_{12}$ due to the flat avoided-crossing filler modes," Phys. Rev. B **91**, 144304 (2015).
[15] J. An, A. Subedi, and D. Singh, "Ab initio phonon dispersions for PbTe," Solid State Communications **148**, 417–419 (2008).
[16] O. Delaire, J. Ma, K. Marty, A. F. May, M. A. McGuire, M.-H. Du, D. J. Singh, A. Podlesnyak, G. Ehlers, M. D. Lumsden, and B. C. Sales, "Giant anharmonic phonon scattering in PbTe," Nature Materials **10**, 614–619 (2011).
[17] T. Shiga, J. Shiomi, J. Ma, O. Delaire, T. Radzynski, A. Lusakowski, K. Esfarjani, and G. Chen, "Microscopic mechanism of low thermal conductivity in lead telluride," Phys. Rev. B **85**, 155203 (2012).
[18] Z. Tian, J. Garg, K. Esfarjani, T. Shiga, J. Shiomi, and G. Chen, "Phonon conduction in PbSe, PbTe, and $PbTe_{1-x}Se_x$ from first-principles calculations," Phys. Rev. B **85**, 184303 (2012).
[19] J.-A. Dolyniuk, B. Owens-Baird, J. Wang, J. V. Zaikina, and K. Kovnir, "Clathrate thermoelectrics," Materials Science and Engineering: R: Reports **108**, 1–46 (2016).
[20] M. Rull-Bravo, A. Moure, J. F. Fernández, and M. Martín-González, "Skutterudites as thermoelectric materials: revisited," RSC Adv. **5**, 41653–41667 (2015).
[21] J. M. Law, H.-J. Koo, M.-H. Whangbo, E. Brücher, V. Pomjakushin, and R. K. Kremer, "Strongly correlated one-dimensional magnetic behavior of $NiTa_2O_6$," Phys. Rev. B **89**, 014423 (2014).
[22] A. B. Christian, S. H. Masunaga, A. T. Schye, A. Rebello, J. J. Neumeier, and Y.-K. Yu, "Magnetic field influence on the Néel, dimer, and spin-liquid states of the low-dimensional antiferromagnets $NiTa_2O_6$ and $CoSb_2O_6$," Phys. Rev. B **90**, 224423 (2014).
[23] A. B. Christian, A. Rebello, M. G. Smith, and J. J. Neumeier, "Local and long-range magnetic order of the spin $-\frac{3}{2}$ system $CoSb_2O_6$," Phys. Rev. B **92**, 174425 (2015).
[24] A. B. Christian, C. D. Hunt, and J. J. Neumeier, "Local and long-range order and the influence of applied magnetic field on single-crystalline $NiSb_2O_6$," Phys. Rev. B **96**, 024433 (2017).
[25] A. B. Christian, A. T. Schye, K. O. White, and J. J. Neumeier, "Magnetic, thermal, and optical properties of single-crystalline $CoTa_2O_6$ and $FeTa_2O_6$ and their anisotropic magnetocaloric effect," Journal of Physics: Condensed Matter **30**, 195803 (2018).
[26] N. Prasai, A. B. Christian, J. J. Neumeier, and J. L. Cohn, "Resonant scattering of phonons in the quasi-one-dimensional spin-chain compounds AB_2O_6 (A = Ni, Co; B = Sb, Ta)," Phys. Rev. B **98**, 134449 (2018).
[27] W. Cochran, "Crystal Stability and the Theory of Ferroelectricity," Phys. Rev. Lett. **3**, 412–414 (1959).
[28] P. B. Klein and R. K. Chang, "Comparison of second-order Raman scattering measurements with a phonon density-of-states calculation in GaSb," Phys. Rev. B **14**, 2498–2502 (1976).
[29] Y. C. Cheng, C. Q. Jin, F. Gao, X. L. Wu, W. Zhong, S. H. Li, and P. K. Chu, "Raman scattering study of zinc blende and wurtzite ZnS," Journal of Applied Physics **106**, 123505 (2009).
[30] R. Hildebrandt, M. Seifert, J. George, S. Blaurock, S. Botti, H. Krautscheid, M. Grundmann, and C. Sturm, "Determination of acoustic phonon anharmonicities via second-order Raman scattering in CuI," New Journal of Physics **25**, 123022 (2023).
[31] P. G. Klemens, "Anharmonic Decay of Optical Phonons," Phys. Rev. **148**, 845–848 (1966).
[32] M. Balkanski, R. F. Wallis, and E. Haro, "Anharmonic effects in light scattering due to optical phonons in silicon," Phys. Rev. B **28**, 1928–1934 (1983).
[33] Y. Tian, S. Jia, R. J. Cava, R. Zhong, J. Schneeloch, G. Gu, and K. S. Burch, "Understanding the evolution of anomalous anharmonicity in $Bi_2Te_{3-x}Se_x$," Phys. Rev. B **95**, 094104 (2017).
[34] F. F. Y. Wang and K. P. Gupta, "Phase transformation in the oxides," Metallurgical Transactions **4**, 2767–2779 (1973).
[35] R. Cowley, "Structural phase transitions I. Landau theory," Advances in Physics **29**, 1–110 (1980).
[36] M. Fujimoto, The physics of structural phase transitions, 2nd ed. (Springer New York, New York 2005).
[37] T. R. Hart, R. L. Aggarwal, and B. Lax, "Temperature Dependence of Raman Scattering in Silicon," Phys. Rev. B **1**, 638–642 (1970).
[38] E. Granado, A. García, J. A. Sanjurjo, C. Rettori, I. Torriani, F. Prado, R. D. Sánchez, A. Caneiro, and S. B. Oseroff, "Magnetic ordering effects in the Raman spectra of $La_{1-x}Mn_{1-x}O_3$," Phys. Rev. B **60**, 11879–11882 (1999).
[39] C. Kant, J. Deisenhofer, T. Rudolf, F. Mayr, F. Schrettle, A. Loidl, V. Gnezdilov, D. Wulferding, P. Lemmens, and V. Tsurkan, "Optical phonons, spin correlations, and spin-phonon coupling in the frustrated pyrochlore magnets $CdCr_2O_4$ and $ZnCr_2O_4$," Phys. Rev. B **80**, 214417 (2009).
[40] N. Khan, D. Kumar, S. Semwal, Y. Shemerliuk, B. Büchner, K. Pal, S. Aswartham, and P. Kumar, "Short and long-range magnetic ordering and emergent topological transition in $(Mn_{1-x}Ni_x)_2P_2S_6$," Scientific Reports **15** (2025), 10.1038/s41598-025-88586-0.
[41] W. H. Baur, "Rutile type derivatives," Zeitschrift für Kristallographie - Crystalline Materials **209**, 143–150 (1994).
[42] R. A. Parker, "Static Dielectric Constant of Rutile (TiO_2), 1.6-1060°K," Phys. Rev. **124**, 1719–1722 (1961).
[43] J. G. Traylor, H. G. Smith, R. M. Nicklow, and M. K. Wilkinson, "Lattice Dynamics of Rutile," Phys. Rev. B **3**, 3457–3472 (1971).
[44] G. A. Samara and P. S. Peercy, "Pressure and Temperature Dependence of the Static Dielectric Constants and Raman Spectra of TiO_2 (Rutile)," Phys. Rev. B **7**, 1131–1148 (1973).
[45] L.-H. Ni, Y. Liu, Z.-H. Ren, C.-L. Song, and G.-R. Han, "Strain-induced ferroelectric phase transitions in incipient ferroelectric rutile TiO_2," Chinese Physics B **20**, 106102 (2011).
[46] R. T. Bate, D. L. Carter, and J. S. Wrobel, "Paraelectric Behavior of PbTe," Phys. Rev. Lett. **25**, 159–162 (1970).
[47] H. Alperin, S. Pickart, J. Rhyne, and V. Minkiewicz, "Softening of the transverse-optic mode in PbTe," Physics Letters A **40**, 295–296 (1972).
[48] K. M. O. Jensen, E. S. Božin, C. D. Malliakas, M. B. Stone, M. D. Lumsden, M. G. Kanatzidis, S. M. Shapiro, and S. J. L. Billinge, "Lattice dynamics reveals a local symmetry breaking in the emergent dipole phase of PbTe," Phys. Rev. B **86**, 085313 (2012).
[49] W. Jantsch, "Dielectric properties and soft modes in semiconducting (pb, sn, ge)te," in Dynamical Properties of IV-VI Compounds (Springer Berlin Heidelberg, 1983) p. 1–50.
[50] S. Karmakar, B. Mukherjee, A. B. Garg, D. S. Gavali, R. Thapa, S. Banerjee, G. D. Mukherjee, A. Haque, and D. Behera, "Structural Metamorphosis and Band Dislocation of Trirutile $NiTa_2O_6$ under Compression," The Journal of Physical Chemistry C **126**, 4106–4117 (2022), https://doi.org/10.1021/acs.jpcc.1c10896.
[51] J. F. Scott, "Soft-mode spectroscopy: Experimental studies of structural phase transitions," Rev. Mod. Phys. **46**, 83–128 (1974).
[52] E. K. Salje and U. Bismayer, "Hard mode spectroscopy: The concept and applications," Phase Transitions **63**, 1–75 (1997), https://doi.org/10.1080/01411599708228789.
[53] William B. White, "The structure of particles and the structure of crystals: information from vibrational spectroscopy," JCPR **006**, 1–9 (2005).
[54] M. Deluca and A. Gajovic, "Raman spectroscopy of nanostructured ferroelectric materials," in Nanoscale Ferroelectrics and Multiferroics (John Wiley Sons, Ltd, 2016) Chap. 11, pp. 325–374,

Supplementary Material
Soft phonon mode as the origin of the reduced thermal conductivity in Ta-based trirutiles

R. Tartaglia,[1] A. F. Lima,[2] N. Prasai,[3] A. B. Christian,[4] J. J. Neumeier,[4] J. L. Cohn,[3] and E. Granado[1]

[1]*Universidade Estatual de Campinas (UNICAMP), Instituto de Física Gleb Wataghin, Campinas, São Paulo 13083-859, Brazil**

[2]*Departamento de Física do Campus de Itabaiana, Universidade Federal de Sergipe, Itabaiana, Sergipe 49510-200, Brazil*

[3]*Department of Physics, University of Miami, Coral Gables, Florida 33124, USA*

[4]*Department of Physics, Montana State University, Bozeman, Montana 59717, USA*

S1. DENSITY FUNCTIONAL THEORY CALCULATIONS

Phonon calculations were performed using DFT through the direct force constant method [1, 2] implemented in the CASTEP code (version 23.1) [3]. In the direct-force constant method, a supercell approach is adopted, where atoms are displaced from their original positions in the limit of the harmonic approximation. The generalized gradient approximation for solids [4] was employed as the exchange-correlation functional, which has satisfactorily described the lattice vibration of crystals [5, 6]. A supercell with dimensions $2 \times 2 \times 2$ was built using relaxed values starting from the experimental lattice parameters and atomic positions of the tetragonal unit cell of the compounds [7, 8]. The limited-memory Broyden–Fletcher–Goldfarb–Shannon algorithm was used to perform the electronic self-consistency calculation with convergence at 5×10^{-6} eV, forces smaller than 0.01 eV/$\mathring{A}$ acting on each atom, and a maximum atomic displacement of 0.50×10^{-1} $\mathring{A}$. The Kohn–Sham orbitals were represented by plane waves with a cut-off energy of 353.74 eV (medium basis set accuracy). The interaction between the nuclear and valence electrons was described by ultrasoft pseudopotentials, and the k-points grid sampling was set to $8 \times 8 \times 4$. No imaginary frequencies were found, indicating the stability of the simulated crystal structures and the accuracy of the calculation parameters adopted [2].

S2. SAMPLE GROWTH

$NiSb_2O_6$ and $ZnSb_2O_6$ single crystals were grown via the chemical vapor transport method, whereas $NiTa_2O_6$ and $CoTa_2O_6$ were synthesized using the optical floating zone technique. Detailed descriptions of both processes can be found elsewhere [9–12]. All crystals have a dark and opaque color, except $NiTa_2O_6$, which is yellowish and semitransparent. The surface dimensions of the employed $NiSb_2O_6$, $NiTa_2O_6$, $ZnSb_2O_6$, and $CoTa_2O_6$ samples are 1.1×0.6 mm^2, 1.2×0.9 mm^2, 1.6×1.0 mm^2, and 0.6×0.6 mm^2 respectively. For $CoTa_2O_6$ and $ZnSb_2O_6$, the *ab* surfaces were used, and for $NiTa_2O_6$ and $NiSb_2O_6$ we used the faces *ac* and $a'c$, respectively, with a' corresponding to the direction along the diagonal of the tetragonal plane.

S3. RAMAN SCATTERING EXPERIMENTS

The samples were glued with silver paint on the cold finger of a closed-cycle He cryostat with a base temperature of 15 K (above T_N for all magnetic samples), with their flat surfaces nearly perpendicular to the direction of the incident beam in a quasi-backscattering configuration. Linearly polarized Raman measurements were performed on a Jobin Yvon T64000 triple 1800 mm^{-1} grating spectrometer equipped with a LN_2-cooled multichannel CCD detector, using a λ = 532 nm excitation line from a Cobolt 08-DPL diode laser. The laser power was set to 70 mW for all the measurements, which showed negligible heating effect (less than 5 K, estimated from the ratio between Anti-Stokes and Stokes scattering of $NiTa_2O_6$) and focused into a spot of $\sim$ 70 μm. All spectra were corrected to account for the thermal population of the phonons to extract the temperature dependence of the Raman response $\chi''(T) = I(T)/(n+1)$, where $I(T)$ is the intensity of the measured spectrum and n is the Bose-Einstein distribution [13].

* Present address: Brazilian Synchrotron Light Laboratory (LNLS), Brazilian Center for Research in Energy and Materials (CNPEM), Campinas, São Paulo 13083-970, Brazil; rodolfo.souza@lnls.br

S4. SYMMETRY ANALYSIS AND PHONON ASSIGNMENT

All the investigated compounds crystallize in the tetragonal space group $P4_2/mnm$, and none exhibits a structural phase transition down to the lowest measured temperature [14–16]. Consequently, all the calculations were done considering the $P4_2/mnm$ space group. Figure S1(a) and S1(b) show the phonon dispersion relation (left panel) and phonon density of states (right panel) for $NiTa_2O_6$ and $NiSb_2O_6$, respectively. No negative phonon frequencies were found, consistent with the stability of the structure and indicating the robustness of the calculations. As expected, the high-frequency region is dominated by oxygen vibrations, while the other heavy elements contribute mainly to vibrations below 350 cm^{-1}.

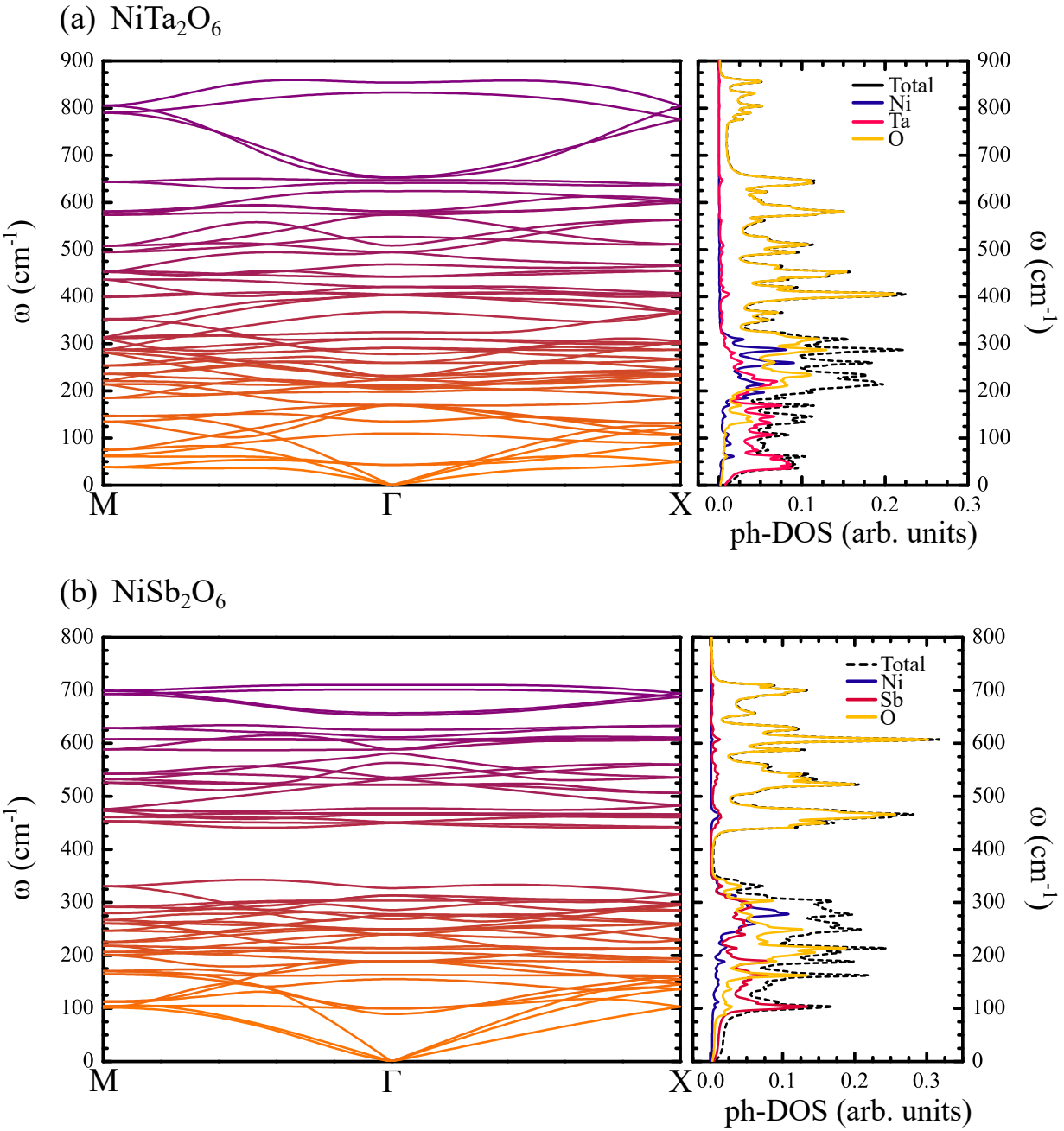

FIG. S1. Calculated phonon dispersion relation along $M-\Gamma-X$ directions of the Brillouin zone (left panel) and phonon density of states (right panel) for (a) $NiTa_2O_6$ and (b) $NiSb_2O_6$. In the right panels, dashed black lines correspond to the total density of states, while purple, pink, and yellow lines correspond to Ni, Ta or Sb, and O partial density of states.

For this structure, a total of 54 phonon modes are predicted [17], from which 16 modes are Raman active with the following

decomposition:

$$\Gamma_{\text{Raman}} = 4A_{1g} + 2B_{1g} + 4B_{2g} + 6E_g.$$

In Table S1, we present the expected phonon modes for the specific polarizations measured in each compound with their corresponding Raman tensors to help the assignment.

TABLE S1. Polarization selection rules for AB_2O_6 (A = Ni, Co, Zn; B = Sb, Ta) following Porto's notation [18]. The Raman tensor of each mode is also given.

Polarization	Raman active modes	Measured compound
$\bar{X}(YZ)X$	E_g	$NiTa_2O_6$
$\bar{X}(ZZ)X$	A_{1g}	
$\bar{Z}(XY)Z$	B_{2g}	$CoTa_2O_6$ and $ZnSb_2O_6$
$\bar{Z}(YY)Z$	A_{1g}, B_{1g}	
$\bar{Z}(X'Y')Z$	B_{1g}	
$\bar{Z}(X'X')Z$	A_{1g}, B_{2g}	
$\bar{X}'(ZY')X'$	E_g	$NiSb_2O_6$
$\bar{X}'(Y'Y')X'$	A_{1g}, B_{2g}	

Raman Tensors:

$$A_{1g} \rightarrow \begin{pmatrix} a & 0 & 0 \\ 0 & a & 0 \\ 0 & 0 & 0 \end{pmatrix} \quad ; \quad B_{1g} \rightarrow \begin{pmatrix} c & 0 & 0 \\ 0 & -c & 0 \\ 0 & 0 & 0 \end{pmatrix}$$

$$B_{2g} \rightarrow \begin{pmatrix} 0 & d & 0 \\ d & 0 & 0 \\ 0 & 0 & 0 \end{pmatrix} \quad ; \quad E_g \rightarrow \begin{pmatrix} 0 & 0 & 0 \\ 0 & 0 & e \\ 0 & e & 0 \end{pmatrix}, \begin{pmatrix} 0 & 0 & -e \\ 0 & 0 & 0 \\ e & 0 & 0 \end{pmatrix}$$

Figure S2 exhibits the polarized Raman spectra at 15 K for all samples with different polarizations of the incident and scattered photons, following Porto's notation [18]. X, Y, and Z correspond to the a, b, and c crystallographic directions, while X' and Y' are along the [110] and [1$\bar{1}$0], respectively, corresponding to the two diagonals of the tetragonal plane. The spectra are comparable to those obtained previously for trirutile compounds [19–26].

In Table S2, we present the calculated Raman active phonon frequencies with their respective symmetries, alongside the measured ones at 15 K and room temperature for $NiTa_2O_6$ and $NiSb_2O_6$. As can be seen, the comparison between theoretical and observed values for $NiTa_2O_6$ shows a satisfactory agreement. In contrast, the same level of agreement is not obtained for $NiSb_2O_6$. For $CoTa_2O_6$ and $ZnSb_2O_6$, only the measured values are given. We also present the phonon frequencies previously measured in polycrystalline samples at room temperature [22], which agree well with the ones obtained in this work.

By analyzing the spectra of Figs. S2(a) - S2(d) in light of the symmetry analysis summarized in Table S1, it is noticed that the polarization selection rules of first-order phonons are not rigorously satisfied by any of the investigated compounds. In fact, most observed modes are visible in all investigated polarizations for each sample. Such polarization leakage occurs for most but not all observed features. For instance, for $CoTa_2O_6$, the low-frequency features observed between ~ 60 and 120 cm^{-1} due to second-order Raman scattering show a very marked polarization dependence [see Fig. S2(c)]. This is remarkable and the opposite of the expected behavior. First-order phonons are associated with only a single symmetry and irreducible Raman susceptibility tensor, with sharp polarization dependence. In contrast, second-order features are associated with tensor products that may be decomposed in more than one irreducible representation [27–29].

Similar depolarization effects were previously reported in other trirutiles [19, 23] and may be associated with structural defects such as ionic vacancies or antisite disorder to some level. In view of these considerations, the polarization analysis of the observed phonon modes is not sufficient to identify unambiguously the symmetry of the phonon peaks in Fig. S2. However, it still provides useful pieces of information. Employing the same methodology of Ref. [19] (combine polarization analysis with DFT-based structural dynamic calculations), and prior phonon assignments for compounds of the same family led us to reasonably identify the symmetry of the observed phonon modes. The final assignment is given in Table S2.

For the spectra taken at the (100) surface of our $NiTa_2O_6$ crystal, we expect to observe E_g or A_{1g} modes in $\bar{X}(YZ)X$ or $\bar{X}(ZZ)X$ polarizations, respectively. The phonon modes around 241, 484, 648 cm^{-1} and 694 cm^{-1} are stronger in $\bar{X}(ZZ)X$ polarization, and their intensities decrease significantly in $\bar{X}(YZ)X$, favoring a A_{1g} symmetry. The remaining observed modes are ascribed to either E_g, B_{1g}, or B_{2g} modes, depending on the comparison with the calculated phonon energies (see Table S2). For the spectra taken at the (001) surface of $CoTa_2O_6$ [Fig. S2(c)], all observed first-order peaks can be mapped out to those observed in $NiTa_2O_6$ [Fig. S2(a)], and therefore these peaks are immediately identified (see Table S2).

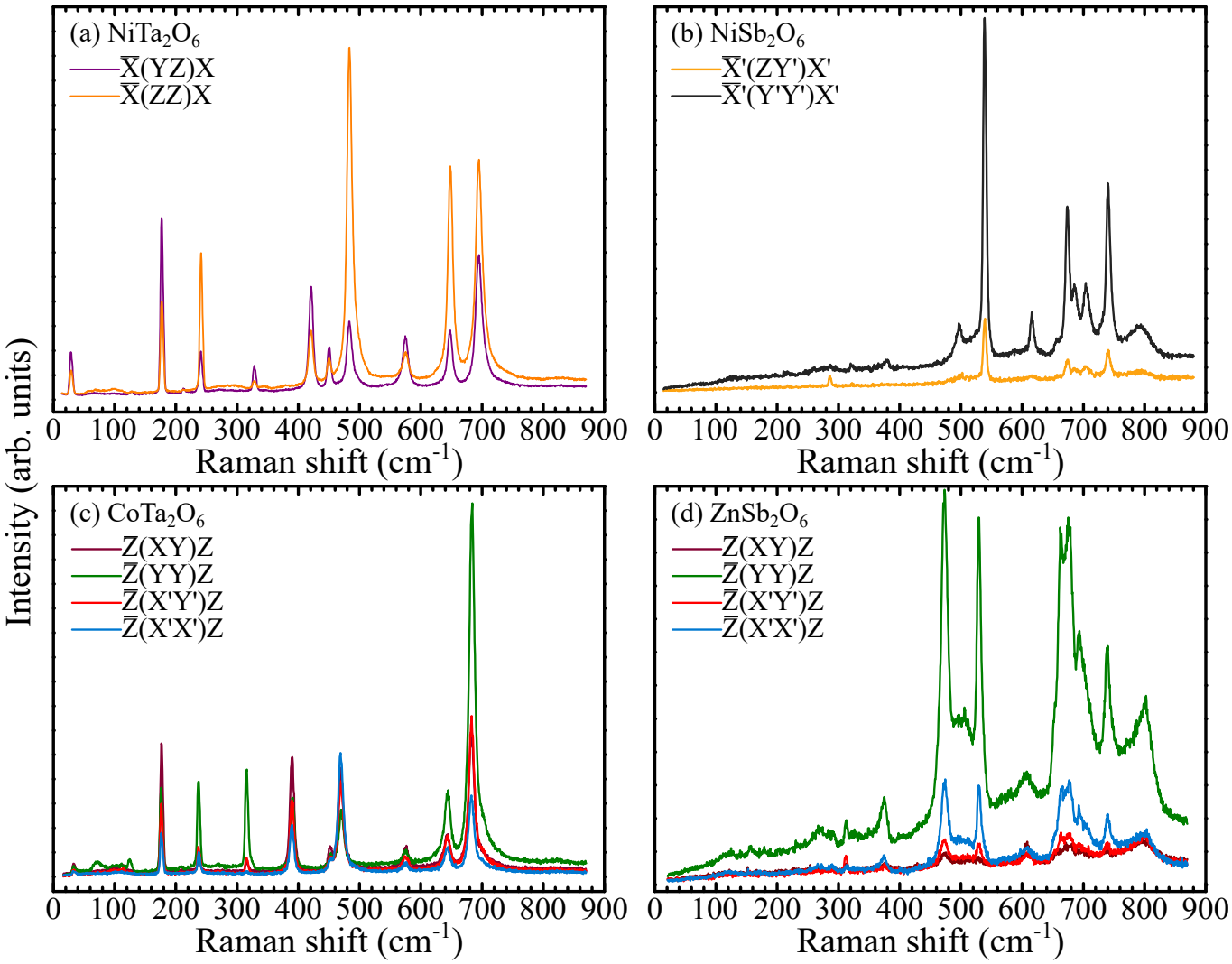

FIG. S2. Polarized Raman spectra at 15 K of (a) $NiTa_2O_6$, (b) $NiSb_2O_6$, (c) $CoTa_2O_6$, and (d) $ZnSb_2O_6$ compounds for different polarizations following Porto's notation [18].

The symmetry analysis for Sb-based compounds is even more challenging than for $CoTa_2O_6$. Analyzing Figs. S2(b) and S2(d), we see an overall reduction in the intensity of all modes when changing polarization. However, we can still obtain some insights for a few phonon modes from it. For $NiSb_2O_6$, the mode around 284 cm^{-1} is present in $\bar{Y}'(ZX')Y'$ but not in $\bar{Y}'(X'X')Y'$, and, according to Table S1, should be an E_g mode. The contrary happens for the modes around 378, and 617 cm^{-1}, indicating that they have A_{1g} or B_{2g} symmetry. For $ZnSb_2O_6$, the symmetry rules can be applied to the modes around 312 and 375 cm^{-1}. The 312 cm^{-1} mode is more pronounced in $\bar{Z}(YY)Z$ and $\bar{Z}(X'Y')Z$, suggesting it has B_{1g} symmetry. The other one exhibits greater intensity in $\bar{Z}(YY)Z$ and $\bar{Z}(X'X')Z$, indicating that it is an A_{1g} mode.

TABLE S2. Calculated and observed Raman-active phonon modes in cm^{-1} at 15 K and room temperature (RT) for $NiTa_2O_6$ and $NiSb_2O_6$ using the tetragonal space group $P4_2/mnm$ and experimental nonrelaxed structural parameters as inputs. For $CoTa_2O_6$ and $ZnSb_2O_6$, only the observed frequencies are shown. We also present the observed frequencies at RT taken from Ref. [22] for comparison.

	$NiTa_2O_6$				$CoTa_2O_6$				$NiSb_2O_6$					$ZnSb_2O_6$		
Symmetry	Calculated	Observed			Observed			Symmetry	Calculated	Observed			Observed			
		15 K	RT	RT [22]	15 K	RT	RT [22]			15 K	RT	RT [22]	15 K	RT	RT [22]	
$E_g^{(1)}$	43	29	40		34	42		$B_{1g}^{(1)}$	89							
$B_{1g}^{(1)}$	135	128	130	132	125	127	130	$E_g^{(1)}$	100							
$E_g^{(2)}$	170	177	178	179	177	177	177	$E_g^{(2)}$	188							222
$B_{2g}^{(1)}$	207	213	211	211	208		204	$B_{2g}^{(1)}$	239				268	268	253	
$A_{1g}^{(1)}$	229	241	240		237	235	234	$E_g^{(3)}$	240	284	284	282	290	290	283	
$E_g^{(3)}$	232							$B_{1g}^{(2)}$	275	318	318	319	312	314	310	
$B_{1g}^{(2)}$	325	330	330	330	316	316	318	$A_{1g}^{(1)}$	286	378	378		375	376	317	
$E_g^{(4)}$	404	421	417	416	389	386	386	$E_g^{(4)}$	450	499	498	465	474	474	435	
$E_g^{(5)}$	443	451	452	455	451	450		$A_{1g}^{(2)}$	477	540	539	535	530	530	526	
$A_{1g}^{(2)}$	469	484	479	478	469	466	462	$E_g^{(5)}$	522							
$B_{2g}^{(2)}$	508							$B_{2g}^{(2)}$	535	617	616	611	606	606	603	
$E_g^{(6)}$	574	576	583	570	575	580		$E_g^{(6)}$	588	675	673	669	663	661	658	
$A_{1g}^{(3)}$	641	648	653	650	643	645	647	$A_{1g}^{(3)}$	611	688	685		677	675		
$B_{2g}^{(3)}$	647							$B_{2g}^{(3)}$	625	706	704		695	694		
$A_{1g}^{(4)}$	652	694	697	697	682	684	684	$A_{1g}^{(4)}$	657	742	741	736	740	738	735	
$B_{2g}^{(4)}$	854							$B_{2g}^{(4)}$	710	792	790		807	803		

[1] K. Parlinski, Z. Q. Li, and Y. Kawazoe, First-Principles Determination of the Soft Mode in Cubic ZrO_2, Phys. Rev. Lett. **78**, 4063 (1997).

[2] I. Pallikara, P. Kayastha, J. M. Skelton, and L. D. Whalley, The physical significance of imaginary phonon modes in crystals, Electronic Structure **4**, 033002 (2022).

[3] S. J. Clark, M. D. Segall, C. J. Pickard, P. J. Hasnip, M. I. J. Probert, K. Refson, and M. C. Payne, First principles methods using CASTEP, Zeitschrift für Kristallographie - Crystalline Materials **220**, 567 (2005).

[4] J. P. Perdew, A. Ruzsinszky, G. I. Csonka, O. A. Vydrov, G. E. Scuseria, L. A. Constantin, X. Zhou, and K. Burke, Restoring the Density-Gradient Expansion for Exchange in Solids and Surfaces, Phys. Rev. Lett. **100**, 136406 (2008).

[5] I. Carvalho, A. Lima, and M. Lalic, Ab initio study of the phonon and thermodynamic properties of the scheelite MWO_4 (M = Ba, Sr or Ca) compounds, Solid State Communications **333**, 114290 (2021).

[6] A. B. Garg, A. Liang, D. Errandonea, P. Rodríguez-Hernández, and A. Muñoz, Monoclinic–triclinic phase transition induced by pressure in fergusonite-type $YbNbO_4$, Journal of Physics: Condensed Matter **34**, 174007 (2022).

[7] H. Müller-Buschbaum and R. Wichmann, Kristallstrukturuntersuchung an $NiTa_2O_6$-Einkristallen Ein Beitrag zur Systematik geordneter und ungeordneter Oxometallate: AB_2O_6 und ABO_4, Zeitschrift für anorganische und allgemeine Chemie **536**, 15 (1986).

[8] M. Weil, R. Mathieu, P. Nordblad, and S. A. Ivanov, Crystal growth experiments in the systems Ni_2MSbO_6 (M = Sc, In) using chemical vapour transport reactions: Ni_2InSbO_6 and $NiSb_2O_6$ crystals in the millimetre range, Crystal Research and Technology **49**, 142 (2014).

[9] A. B. Christian, S. H. Masunaga, A. T. Schye, A. Rebello, J. J. Neumeier, and Y.-K. Yu, Magnetic field influence on the Néel, dimer, and spin-liquid states of the low-dimensional antiferromagnets $NiTa_2O_6$ and $CoSb_2O_6$, Phys. Rev. B **90**, 224423 (2014).

[10] A. B. Christian, A. Rebello, M. G. Smith, and J. J. Neumeier, Local and long-range magnetic order of the spin $-\frac{3}{2}$ system $CoSb_2O_6$, Phys. Rev. B **92**, 174425 (2015).

[11] A. B. Christian, C. D. Hunt, and J. J. Neumeier, Local and long-range order and the influence of applied magnetic field on single-crystalline $NiSb_2O_6$, Phys. Rev. B **96**, 024433 (2017).

[12] A. B. Christian, A. T. Schye, K. O. White, and J. J. Neumeier, Magnetic, thermal, and optical properties of single-crystalline $CoTa_2O_6$ and $FeTa_2O_6$ and their anisotropic magnetocaloric effect, Journal of Physics: Condensed Matter **30**, 195803 (2018).

[13] T. P. Devereaux and R. Hackl, Inelastic light scattering from correlated electrons, Rev. Mod. Phys. **79**, 175 (2007).

[14] J. Reimers, J. Greedan, C. Stager, and R. Kremer, Crystal structure and magnetism in $CoSb_2O_6$ and $CoTa_2O_6$, Journal of Solid State Chemistry **83**, 20 (1989).

[15] H. Ehrenberg, G. Wltschek, J. Rodriguez-Carvajal, and T. Vogt, Magnetic structures of the tri-rutiles $NiTa_2O_6$ and $NiSb_2O_6$, Journal of Magnetism and Magnetic Materials **184**, 111 (1998).

[16] E. Tetsi, AB_2O_6 oxides: Potential Thermoelectric and Magnetic Materials, Phd thesis, University of Liverpool, Liverpool, Merseyside (2017), available at `https://livrepository.liverpool.ac.uk/id/eprint/3014158`.

[17] E. Kroumova, M. I. Aroyo, J. M. Perez-Mato, A. Kirov, C. Capillas, S. Ivantchev, and H. Wondratschek, Bilbao Crystallographic Server: Useful Databases and Tools for Phase-Transition Studies, Phase Transitions **76**, 155 (2003).

[18] T. C. Damen, S. P. S. Porto, and B. Tell, Raman Effect in Zinc Oxide, Phys. Rev. **142**, 570 (1966).

[19] D. T. Maimone, A. B. Christian, J. J. Neumeier, and E. Granado, Lattice dynamics of ASb_2O_6 (A = Cu, Co) with trirutile structure, Phys. Rev. B **97**, 104304 (2018).

[20] D. T. Maimone, A. B. Christian, J. J. Neumeier, and E. Granado, Coupling of phonons with orbital dynamics and magnetism in $CuSb_2O_6$, Phys. Rev. B **97**, 174415 (2018).

[21] E. Husson, Y. Repelin, H. Brusset, and A. Cerez, Spectres de vibration et calcul du champ de force des antimoniates et des tantalates de structure trirutile, Spectrochimica Acta Part A: Molecular Spectroscopy **35**, 1177 (1979).

[22] H. Haeuseler, Infrared and raman spectra and normal coordinate calculations on trirutile-type compounds, Spectrochimica Acta Part A: Molecular Spectroscopy **37**, 487 (1981).

[23] D. Xu, S. Gao, W. Liu, Y. Liu, Q. Zhou, L. Li, T. Cui, and H. Yuan, The Raman scattering of trirutile structure $MgTa_2O_6$ single crystals grown by the optical floating zone method, RSC Adv. **9**, 839 (2019).

[24] R. Baral, H. S. Fierro, C. Rueda, B. Sahu, A. M. Strydom, N. Poudel, K. Gofryk, F. S. Manciu, C. Ritter, T. W. Heitmann, B. P. Belbase, S. Bati, M. P. Ghimire, and H. S. Nair, Signatures of low-dimensional magnetism and short-range magnetic order in Co-based trirutiles, Phys. Rev. B **100**, 184407 (2019).

[25] S. Karmakar, B. Mukherjee, A. B. Garg, D. S. Gavali, R. Thapa, S. Banerjee, G. D. Mukherjee, A. Haque, and D. Behera, Structural Metamorphosis and Band Dislocation of Trirutile $NiTa_2O_6$ under Compression, The Journal of Physical Chemistry C **126**, 4106 (2022), https://doi.org/10.1021/acs.jpcc.1c10896.

[26] H. Yang, Z. Guo, Z. Xiong, J. Yang, X. Wang, G. Wang, C. Xu, and Z. Li, Bond theory, vibrational spectroscopy, and dielectric responses of trirutile ATa_2O_6 (A = Mg, Ni) microwave ceramics, Ceramics International **50**, 19171 (2024).

[27] M. Cardona, Resonance phenomena, in Light Scattering in Solids II: Basic Concepts and Instrumentation, edited by M. Cardona and G. Güntherodt (Springer Berlin Heidelberg, Berlin, Heidelberg, 1982) pp. 19–178.

[28] R. Merlin, A. Pinczuk, and W. H. Weber, Overview of Phonon Raman Scattering in Solids, in Raman Scattering in Materials Science, edited by W. H. Weber and R. Merlin (Springer Berlin Heidelberg, Berlin, Heidelberg, 2000) pp. 1–29.

[29] P. Sherwood, Vibrational Spectroscopy of Solids (Cambridge University Press, 2011).